Extending the planetary mass function to Earth mass by microlensing at moderately high magnification

Fumio Abe,[1]⋆ Charlotte Airey,[2] Ellen Barnard,[2] Julie Baudry,[3] Christine Botzler,[2] Dimitri Douchin,[4] Matthew Freeman,[2] Patricia Larsen,[2] Anna Niemiec,[5] Yvette Perrott,[6] Lydia Philpott,[7] Nicholas Rattenbury[2] and Philip Yock[2]⋆

[1]*Solar-Terrestrial Environment Laboratory, Nagoya University, Nagoya 464-8601, Japan*
[2]*Department of Physics, University of Auckland, Private Bag 92019, Auckland, New Zealand*
[3]*Département de Physique, Université Paris Sud, Bât 333, F-91403 Orsay Cedex, France*
[4]*Department of Astrophysics, MacQuarie University, NSW 2109, Australia*
[5]*Département de Physique, Ecole Normale Superieue de Cachon, 61, avenue du Président-Wilson, F-94235 Cachan Cedex, France*
[6]*Astrophysics Group, Cavendish Laboratory, JJ Thomson Avenue, Cambridge CB3 OHE, UK*
[7]*Department of Earth and Ocean Sciences, University of British Columbia, Vancouver, BC V6T 1Z4, Canada*

ABSTRACT

A measurement by microlensing of the planetary mass function of planets with masses ranging from $5\,M_\oplus$ to $10\,M_J$ and orbital radii from 0.5 to 10 au was reported recently. A strategy for extending the mass range down to $(1-3)\,M_\oplus$ is proposed here. This entails monitoring the peaks of a few tens of microlensing events with moderately high magnifications with 1–2 m class telescopes. Planets of a few Earth masses are found to produce deviations of ∼5 per cent to the peaks of microlensing light curves with durations ∼(0.7–3) hr in events with magnification ∼100 if the projected separation of the planet lies in the annular region $(0.85-1.2)r_E$. Similar deviations are produced by Earth mass planets in the annular region $(0.95-1.05)r_E$. It is possible that sub-Earths could be detected very close to the *Einstein* ring if they are sufficiently abundant, and also planetary systems with more than one low-mass planet.

Key words: gravitational lensing: micro – planetary systems.

1 INTRODUCTION

Recently, Cassan et al. (2012) conducted a fairly comprehensive census of planets in the Milky Way using the microlensing technique. For planets at orbital radii of 0.5–10 au, they reported that 17^{+6}_{-9} per cent of stars host planets with masses in the range $(0.3-10)\,M_J$, 52^{+22}_{-29} per cent host cool Neptunes with masses $(10-30)\,M_\oplus$, and 62^{+35}_{-37} per cent host super-Earths with masses $(5-10)\,M_\oplus$. The results are encouraging for a discipline so young, but the uncertainties are large for the lower mass planets, and also the measurements do not extend down to planets of Earth mass. In this paper, we attempt to address these problems by proposing a modified strategy for detecting low-mass planets by microlensing.

Our strategy is based on a proposal originally made in 1998 by Griest & Safizadeh for detecting planets in microlensing events of high magnification. High magnification occurs when the source star passes almost directly behind the lens star, so that $\theta_{\min} \ll$

θ_E, or $u_{\min} \ll 1$.[1] These very well aligned events are rarer than normal microlensing events that have magnifications of only a few, but they are easily recognizable because the peak magnification is approximately $\theta_E/\theta_{\min}$ and this is $\gg 1$. Moreover, as Griest and Safizadeh showed, if a planet orbits the lens star, it almost certainly produces a perturbation to the light curve close to the peak of the light curve. It thus appeared possible to search for planets with high efficiency merely by monitoring the peaks of events that had high magnification.

---

[1] Our notation is fairly conventional. In particular, r_E, t_E and t_0 denote the *Einstein* radius, crossing time and time of closest approach between the lens and source stars, and θ_E, $\theta_{\min}$ and θ_s the *Einstein* radius, the impact parameter between the lens and source stars in angular coordinates, and the angular radius of the source star, respectively. We denote by $u_{\min}$ the projected impact parameter in the lens plane between the lens and source stars in units of r_E. Thus, $u_{\min} = \theta_{\min}/\theta_E$. Finally, for planetary events, we denote by q, d and θ the planet-to-star mass ratio, projected separation in units of r_E and axis relative to the source star track, respectively. The fundamental parameter of microlensing, the *Einstein* radius r_E, is defined in Rattenbury et al. (2002).

⋆ E-mail: abe@stelab.nagoya-u.ac.jp (FA); p.yock@xtra.co.nz (PY)

This was noted by several groups (Gaudi, Naber & Sackett 1998; Rhie et al. 2000; Bond et al. 2002; Rattenbury et al. 2002) and subsequently demonstrated to be correct. Since 2002 a steadily growing number of high-magnification events were discovered and alerted each year by the MOA and OGLE collaborations.[2] Several of these events were monitored by 'follow-up' networks[3] and this led to the discoveries of several planets (Udalski et al. 2005; Gould et al. 2006; Gaudi et al. 2008; Bennett et al. 2008; Dong et al. 2009; Janczek et al. 2010; Miyake et al. 2011; Bachelet et al. 2012; Yee et al. 2012; Han et al. 2013), some of the first measurements of planetary abundances (Gould et al. 2006, 2010), and also to a measurement of limb darkening (Fouqué et al. 2010).

A new class of events was also discovered by the MOA and OGLE microlensing collaborations in their quests for high-magnifications events. Both collaborations found events having very high magnifications, of the order of 1000 (e.g. Abe at al. 2004; Dong et al. 2006). When these were first discovered it was natural to assume that they would provide greater sensitivity to planets. This assumption is the subject of this paper.

Our conclusion is that low-mass planets can be efficiently searched for in events with moderately high magnifications of the order of 50–200, and that the greater frequency of these events in comparison to those with higher magnifications lends advantage to monitoring them. However, to take full advantage of their discovery potential, telescopes with apertures in the range 1–2 m would be needed to photometer them with sufficient precision to detect low-mass planets.[4]

Using such telescopes, the planetary mass function of Cassan et al. (2012) may be able to be extended down to Earth mass. Because such planets have special importance in the search for the proverbial 'Earth twin', and because their abundance will constrain theories of planetary formation, it is important to optimize strategies to encompass these planets in observing programmes.

Recently Han (2009) and Han & Kim (2009) examined the sensitivity of the high-magnification technique for detecting planets. However, they did not explicitly examine the sensitivity as a function of magnification, nor did they focus on the lower magnification events considered in this paper. Our results are therefore complementary to theirs.

2 *EINSTEIN* ARCS

Liebes (1964) first suggested that planets might be detected by gravitational microlensing. His analysis was based upon the use of *Einstein* arcs. Fig. 1 shows the well-known geometry of the pair of moving *Einstein* arcs that are formed in a normal microlensing event (Paczynski 1996). For clarity, the radius of the source star (projected to the lens plane) has been greatly exaggerated. Typically, it is of the order of $10^{-3} \times r_{\mathrm{E}}$ and the *Einstein* arcs are of comparable width.

Fig. 1 may be used to understand qualitatively the main features of planet detection in high-magnification events. Straightforward geometrical considerations show that the lengths of the *Einstein*
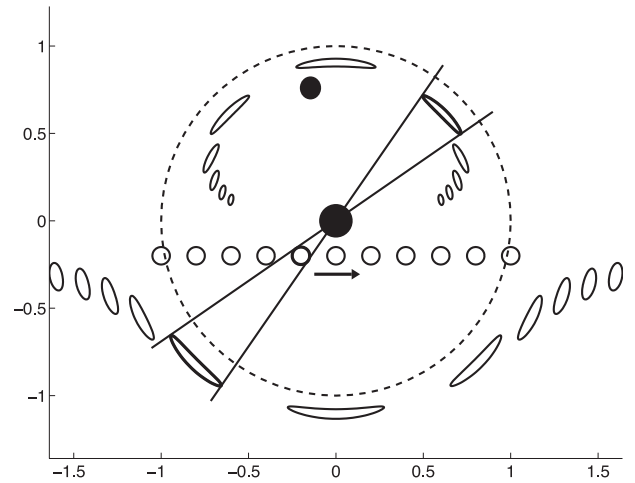
Figure 1. The pair of moving *Einstein* arcs formed in a typical example of gravitational microlensing. The source star is shown as a moving, open circle, and the lens star as a filled, stationary circle. Also shown is a planet in the lens star system that is fairly close to the *Einstein* ring. The units are fractions of r_{E} and the source star radius is scaled to its projected value in the lens plane. The magnitude of r_{E} is ∼2 au in typical Galactic microlensing events. It is therefore reasonable to suppose the presence of a planet close to the ring as shown in the figure. This figure (without the planet) is adapted from Paczynski (1996).

arcs in the lens plane near the time of maximum magnification are $\sim 2\theta_s r_{\mathrm{E}}/\theta_{\min}$. If the lens star hosts a planet, and if the planet is situated fairly close to either the upper or the lower portions of the *Einstein* ring as shown in the figure, then one of the *Einstein* arcs will slide by it during the event, and be perturbed by it. In this way, a planet betrays its presence. The effect is large because the image of the source star is magnified by the lens star, and the magnified image is perturbed by the planet.

If the planet is closer to the *Einstein* ring than the arc length, as shown in the figure, the duration of the planetary perturbation is given by the time required for the arc to slide by the planet. This is easily shown to be $\sim 3\rho t_{\mathrm{E}}$, where $\rho = \theta_s/\theta_{\mathrm{E}}$.[5] The result is independent of $u_{\min}$, and therefore of the peak magnification $A_{\max}$, as $A_{\max} \approx u_{\min}^{-1}$. Higher magnifications produce longer arcs, but they rotate faster, and the slide-by time is unchanged. The magnitudes of the perturbations are surprisingly large, as discussed below. They are positive if the source star trajectory threads the lens star–planet system ($u_{\min} \geq 0$) and vice versa. As expected, they increase (approximately proportionally) with the mass of the planet, and as the planet approaches the *Einstein* ring. We note that these scaling laws differ qualitatively from those found for perturbations caused by planetary caustic crossings (Horne, Snodgrass & Tsapras 2009).

Several examples of computed planetary perturbations may be found in the literature that confirm the above expectations (Rhie et al. 2000; Rattenbury et al. 2002; Bennett et al. 2008). For typical values of $\rho \approx 0.001$ and $t_{\mathrm{E}} \approx 20$ d, planetary perturbations of duration about 1.4 h are predicted. For typical ranges of ρ and t_{E} (see Section 6 below), we expect durations ranging over

~(0.7–3) h. Such perturbations may be conveniently observed from a single observing site.

There are two exceptions to the above. If a planet lies very close to the *Einstein* ring, the difference from the planetless light curve can become large. In this case, the above perturbative picture fails, and a quantitative analysis (as carried out below) is required.
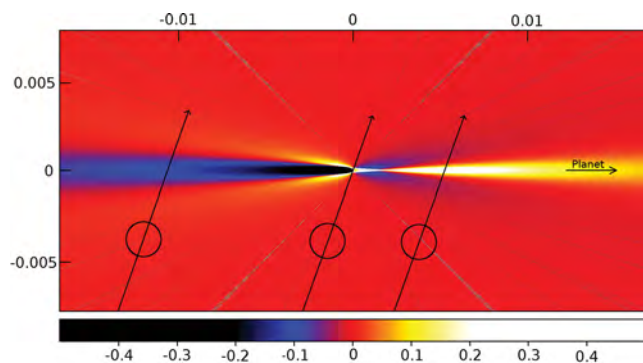
Secondly, for events with very small impact parameters in which the source star passes behind the lens star, the geometry of the moving arcs is different from that depicted in Fig. 1. In these events, a pair of arcs is formed fore-and-aft of the lens, instead of above and below it (Liebes 1964). A planet perturbs both arcs, one after the other, leading to the formation of two very brief spikes of opposing polarities on the light curve. Examples of such spikes have been observed and modelled (Dong et al. 2009; Han & Kim 2009; Janczek et al. 2010). Furthermore, examples are displayed below.

3 MAGNIFICATION MAPS

Wambsganss (1997) originally used magnification maps to demonstrate the detectability of planets by gravitational microlensing. In this method, rays are shot from the observer, which is treated as a point source, through the lens in the thin-lens approximation to the source plane to form a 'magnification map' that is sampled by the moving source star.

Fig. 2 above shows a magnification map for a typical high-magnification event. The lens consists of a star at the origin and a planet on the positive *x*-axis at a distance d of 0.9. The planet-to-star mass ratio q is 3×10^{-5}. This corresponds to a super-Earth of about three Earth masses if the lens star is an M or K dwarf. The map shows the pixel-by-pixel fractional perturbation caused by the planet. It is seen to be approximately $\sim +10$ per cent for a large region extending to $x \sim +0.015$ towards the planet, and ~ -10 per cent for a similarly large region extending to $x \sim -0.015$ away from the planet.

Also shown are three possible tracks of a source star at a typical inclination to the star–planet axis. The leftmost track is for a solar-like source star with impact parameter $u_{\min} = -0.01$ or $A_{\max} = 100$. For the central track, the impact parameter $u_{\min} = 0$ and $A_{\max} = 2\theta_E/\theta_s = 2000$ by Liebes's theorem (1964). The righthand track

corresponds to $u_{\min} = +0.005$ and $A_{\max} = 200$. Integrating 'by eye' over the area of the source star indicates that the left-hand and right-hand trajectories with $A_{\max}$ of 100 and 200 yield planetary perturbations approaching -10 per cent and $+10$ per cent, respectively in magnitude.

Perturbations to light curves of the order of 10 per cent are readily detectable when the magnification is ≥ 100, yet perturbations of the above type have not been extensively sought in planet searches to date. It should therefore be possible to increase the current detection rate of planets by making use of the large extent of the regions shown on the left- and right-hand sides of Fig. 2.

At the centre of the map lies the 'stellar caustic'. This is an approximately triangular closed curve of formally infinite magnification extending from the lens star towards the planet with length about 0.002, i.e. approximately the diameter of the source star shown in the figure. The true length of the caustic is 0.0027 (Han 2009) but this is not discernable on the map due to the finite size of the pixels. The caustic provides a means for detecting planets, but source star tracks that traverse it are subject to cancellations from neighbouring areas of opposing polarities. On the other hand, the areas to the left and right of the caustic do not suffer from cancellations to the same extent. In addition, they are longer, and therefore offer the prospect of more numerous traversals in any random sample of events.

Magnification maps similar to that shown in Fig. 2 for heavier or lighter planets, at greater or smaller distances from the *Einstein* ring, yield similar results.

4 LIGHT CURVES

In order to further assess the detectability of low-mass planets, light curves were computed for a range of planet masses and separations. The light curves were generated by subdividing the source plane into three regions. A central region was used to construct the peaks of light curves [approximately two times the full width at half-maximum (FWHM)] at high resolution. A larger region was used to extend the light curves out to $\sim \pm 0.5 t_E$ at moderate resolution, and an outer region was used to further extend them to $\sim \pm 2 t_E$ at low resolution. The pixel size in each region, and the number of rays per pixel, were adjusted to keep numerical noise below the precision of typical data. The wings of the light curves beyond the outermost of the above regions were treated in the single-lens approximation. Limb darkening was included in the linear approximation with a limb darkening coefficient of 0.5. The procedures were checked by comparison with published analyses of several events.

In order for a planetary deviation to be clearly identified on a light curve, it is helpful if both the deviation and also a significant portion of the unperturbed light curve is observed. If we imagine an ideal search being executed with robotically controlled telescopes programmed to monitor the FWHMs of selected events from sites of excellent seeing, then this requirement will favour events for which $A_{\max} \leq 500$. As remarked in Section 2, the duration of a typical planetary deviation is $\sim 3 \rho t_E$, whereas t_{FWHM} is $3.5 t_E / A_{\max}$ (Rattenbury et al. 2002). To sample both the deviation and the unperturbed light curve equally precisely, the deviation should occupy less than half the FWHM. This translates to $A_{\max} \leq 0.5 \rho^{-1}$ or $A_{\max} \leq 500$ for a typical value of $\rho \approx 0.001$.[6] We note however that, in actual practice, the descending branch of the FWHM will tend to be more fully monitored than the ascending branch, and that coverage on

Figure 2. Map of normalized fractional planetary deviations produced by a planetary system consisting of a star at the centre and a planet with $q = 3 \times 10^{-5}$ and $d = 0.9$ to the right. The deviations were computed pixel-by-pixel as the difference in magnification produced by a star with and without a planet, normalized by the magnification without a planet. The coordinates shown are fractions of θ_E. Also shown are typical tracks of a solar-like source star at $\theta \approx 60°$. Moire-like artefacts caused by the use of rectangular pixels are present. They are alternately positive and negative, and have small net effects when integrated over the source star.

---

[6] The corresponding condition when hunting exo-moons orbiting free-floating planets can also be met, but not so easily.

the descending branch may usefully extend beyond the FWHM. We note also that some previously made planetary discoveries have suffered from less than complete coverage of the FWHM.

Fig. 3 shows typical planetary deviations. The planet-to-star mass ratio and separation are the same as those used in Fig. 2. The fractional deviations are plotted for A_{max} equal to 2000, 500, 200, 100 and 50, respectively. The first exhibits the double-spiked structure discussed above, and the others exhibit perturbations of the width and height predicted above. For the last one at $A_{max} = 50$, the requirement that the planet be closer to the *Einstein* ring than the length of the *Einstein* arcs begins to break down, and the width of the perturbation is greater than predicted.

A number of plots similar to those in Fig. 3 were constructed and examined. Fig. 4 shows the dependence of planetary perturbations on impact parameter u_{min}. The parameter u_{min} was chosen as the in-

dependent variable in this plot, rather than the equivalent parameter A_{max} which approximately equals $1/u_{min}$, because u_{min} is uniformly populated in any unbiased sample of events, whereas A_{max} is not.

It is apparent from Fig. 4 that, for all combinations of the other parameters, there is a drop in the fractional deviations for the smallest values of u_{min}, i.e. for the largest magnifications. This is caused by the onset of the 'double-spike' phenomenon discussed above.

Fig. 4 also shows the dependence of a typical planetary perturbation on the angle θ between the planet–star axis and the track of the source star. The dependence is essentially constant for angles larger than $30°$.

The dependence on the source-size parameter $\rho = \theta_s/\theta_E$ is also shown in Fig. 4. For typical events with solar-like source stars in the Galactic bulge, and main sequence *M–K* lens stars lying in the bulge or in the galactic disc, ρ takes on values between about 0.0005 and 0.002. It is seen that planetary deviations are greater for smaller values of ρ, and they are quite low when ρ is as large as 0.005. The latter value is about the minimum possible value of ρ if the source star is a giant.

The dependence of typical planetary perturbations on the planet mass parameter q is displayed in Fig. 5. Here, q was set equal to 1×10^{-5}, 3×10^{-5} or 1×10^{-4}. For each value of q, the value of d was adjusted (in increments of 0.05) to yield a fractional deviation of ∼4 per cent when a solar-like source star with $\rho = 0.001$ was magnified 100 times ($u_{min} = +0.01$). This procedure yielded approximate ranges of the variables q, d, u_{min} and ρ, where planets are likely to be detectable. The value of 4 per cent was chosen as approximately the minimum detectable fractional deviation currently being achieved with 0.3–1.3 m class follow-up telescopes.

The above procedure yielded minimum detectable values of d of ∼0.95, 0.85 and 0.7 for q equal to 1×10^{-5}, 3×10^{-5} and 1×10^{-4}, respectively. For values of d lying outside the *Einstein* ring, the well-known d to $1/d$ symmetry (Griest & Safizadeh 1998) yields maximum detectable values of d of ∼1.05, 1.2 and 1.4, respectively. These limiting values of d agree with those reported by Han (2009), who assumed a minimum detectable fractional deviation of 5 per cent.

An increase in the breadth of the plots in Fig. 5 as q decreases (right to left) is evident. This implies, irrespective of any details,
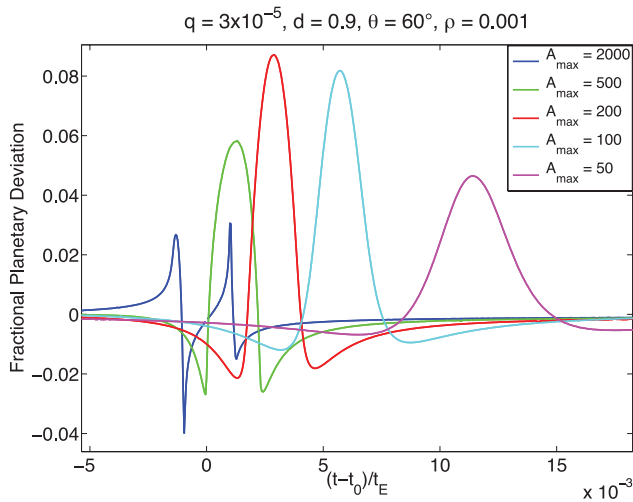
Figure 3. Fractional deviations between light curves with and without a planet for various magnifications. The planet-to-star mass ratio q and separation d are 3×10^{-5} and 0.9, as in Fig. 2, and the angle between the planet–star axis and the track of the source star is $60°$. The impact parameter u_{min} is 0, 0.002, 0.005, 0.01 or 0.02, respectively.
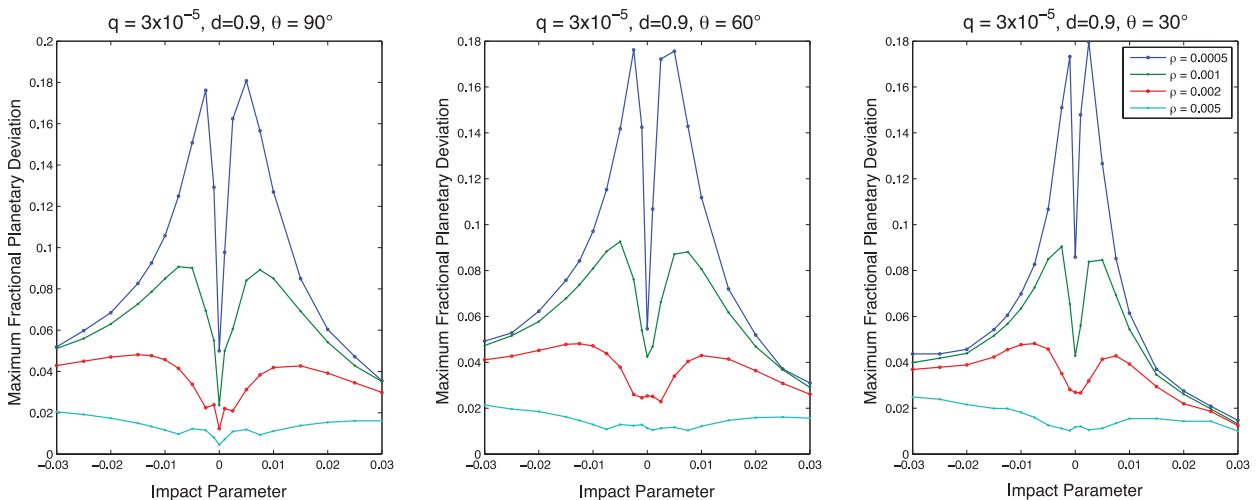
Figure 4. Planetary deviations as a function of impact parameter u_{min} for various source star track angles. For each value of u_{min}, the maximum value of the fractional deviation from the planetless light curve is plotted. The positive values of u_{min} correspond to the source star threading the lens system, and vice versa. The planet-to-star mass ratio and separation are as in Figs 2 and 3.
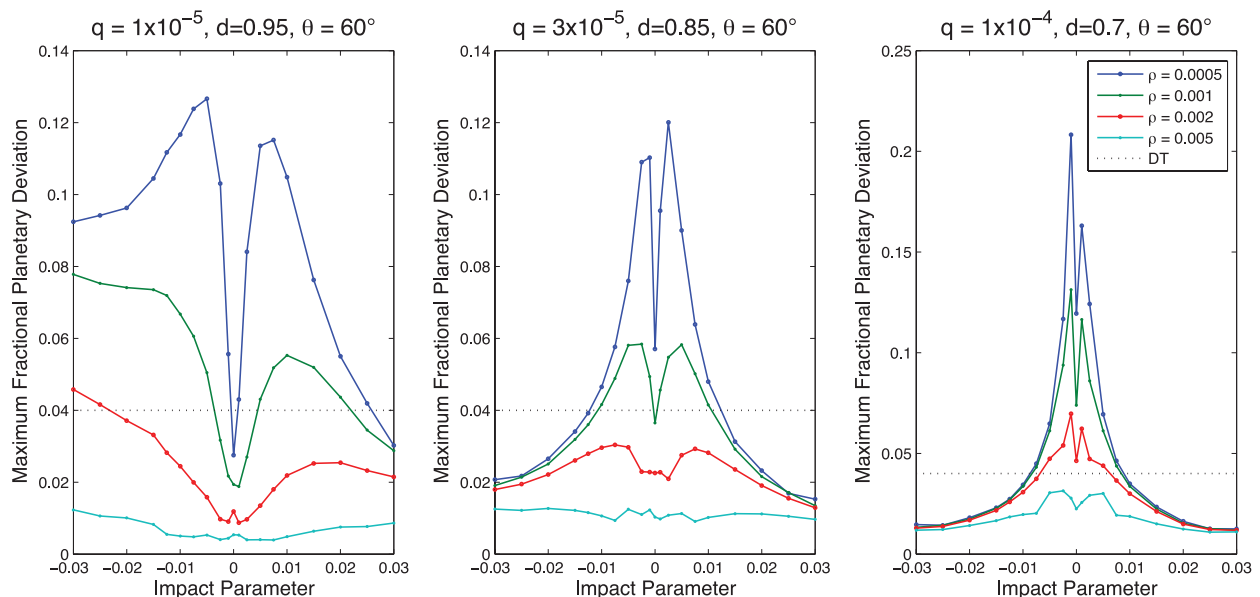
Figure 5. Planetary deviations as a function of impact parameter for various planet masses q and separations d. A detection threshold of 4 per cent at $A_{max} = 100$ was assumed as described in the text. The rising sensitivity at negative u_{min} for a planet at $d = 0.95$ (and to lesser extents for planets at $d = 0.85$ and 0.7) is caused by a cooperative effect between the central and planetary caustics shown in Fig. 6.
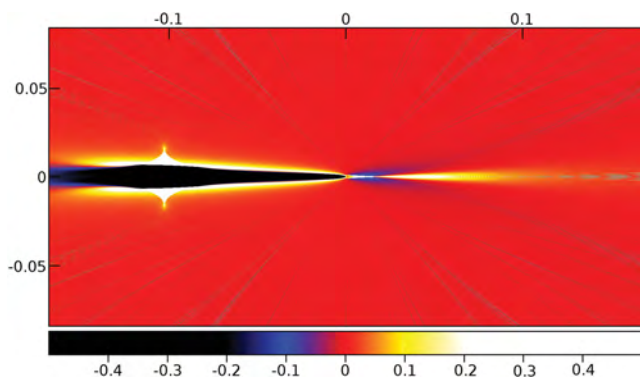
Figure 6. Map of fractional planetary deviations for a planet with $q = 10^{-4}$ and $d = +0.95$ showing enhanced sensitivity at negative values of u_{min} and moderate magnifications.

that very low mass planets with $q \sim 10^{-5}$ and $d \sim 0.95$ will be detectable in events distributed over a wider range of magnifications than heavier planets with $q \sim 10^{-4}$ and $d \sim 0.7$. In hunting for the lowest mass planets it will therefore be advantageous to monitor events with the broadest range of magnifications possible.

We note that the detection efficiencies at the above limiting values of q and d are ~ 67 per cent if only the FWHM's of light curves are monitored intensively. This follows because only those planets with planet–star axes at angles $\geq 30°$ to the track of the source star are probed during the FWHM (Rattenbury et al. 2002).

We note also that the left-hand panel of Fig. 5 exhibits a bias towards negative values of u_{min}. This is caused by a cooperative effect between the stellar caustic at the origin and a pair of planetary caustics above and below the negative x-axis for a planet located just inside the *Einstein* ring, as shown in Fig. 6. A similar effect occurs for planets located just outside the *Einstein* ring and positive values of u_{min}.

These cooperative effects already aided discoveries of planets, in MOA-2009-BLG-266 (Muraki et al. 2011) and OGLE-2012-BLG-

0461 (C. Han, private communication) for example, and they could boost the detection rate of low-mass planets in future events with magnifications of the order of a few to several tens. However, the lower magnifications of these events may need to be compensated by brighter source stars.
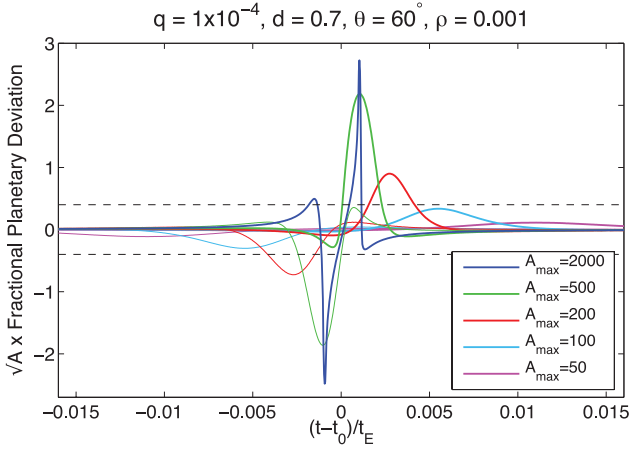
5 STATISTICALLY ADJUSTED PLANETARY DEVIATIONS

The previous discussion can be extended by allowing for the relative precisions with which planetary deviations can be measured at different magnifications. As a first approximation, we assume Poisson statistics for the detected photons in any exposure, and multiply fractional deviations by the square root of amplification to approximate relative detectabilities. The results for the three (q, d) combinations shown in Fig. 5 are reproduced below in Figs 7–9. These include perturbations for negative impact parameters as well as the positive ones shown in Fig. 3. They are almost mirror images of one another (Rattenbury et al. 2002).

The inclusion of the Poisson factor tends to reverse the effect of the diminished deviations shown in Fig. 3 at large magnifications. In Fig. 7, the largest perturbation occurs at $A_{max} = 500$. Although the peak signals at $A_{max} = 2000$ are larger in magnitude, their contributions to χ^2 in a full analysis would be limited by the narrowness of the spikes.

The estimate made in Section 4 of a minimum detectable fractional deviation of 0.04 at $A_{max} = 100$ with telescopes currently in use moves to 0.4 on Figs 7–9. The calculated perturbations at $A_{max} = 100$ are seen to be almost at the threshold, as expected.

The results shown in Figs 8 and 9 for lighter planets closer to the *Einstein* ring show the same trend that was found in Fig. 5. The importance of lower magnification events grows until at $(q, d) = (1 \times 10^{-5}, 0.95)$ events with magnifications from 50 to 500 are seen to provide approximately equal sensitivities on an event-by-event basis, with a slight preference for negative impact parameters over positive ones. When one allows for the greater frequency of events

Figure 7. Statistically adjusted fractional planetary deviations for $(q, d) = (1 \times 10^{-4}, 0.7)$ at various magnifications. The lines at ± 0.4 are the estimated limits of detectability with telescopes currently in use as discussed in the text.
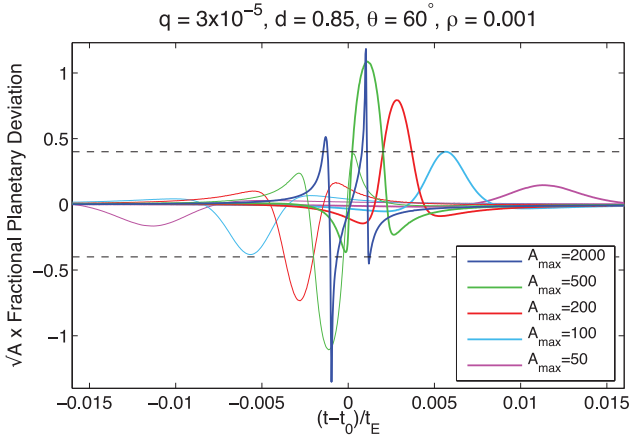
Figure 8. Statistically adjusted perturbations for planets with $(q, d) = (3 \times 10^{-5}, 0.85)$ at various magnifications. Estimated limits of detectability with current telescopes are shown at ± 0.4.
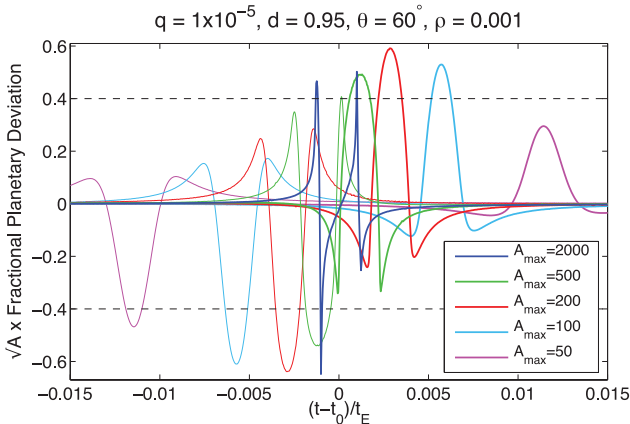
Figure 9. Statistically adjusted perturbations for planets with $(q, d) = (1 \times 10^{-5}, 0.95)$ at various magnifications. The enhancement at negative impact parameters over positive ones results from the cooperative effect between stellar and planetary caustics discussed in Section 4.
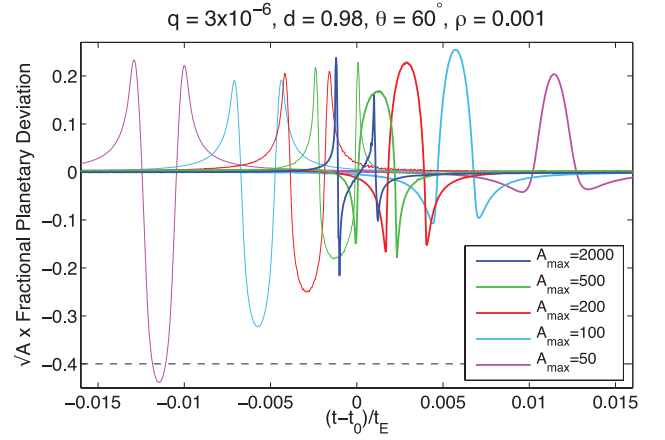
Figure 10. Statistically adjusted perturbations for planets with $(q, d) = (3 \times 10^{-6}, 0.98)$ at various magnifications. The large enhancement at negative impact parameters results from the cooperative effect between stellar and planetary caustics described in Section 4.

with lower magnifications, they are seen to provide the greatest discovery potential.

For planets even closer to the ring, the advantage of working at lower magnification becomes more evident. Fig. 10 shows results for $(q, d) = (3 \times 10^{-6}, 0.98)$. Here, it is seen that the sensitivity to sub-Earths is significant at $A_{\max}$ as low as 50.

Fig. 10 exhibits the best of all worlds. The source star is highly magnified, the planet perturbs the highly magnified image, and the magnification is further enhanced by planetary caustics. Moreover, these properties are predictable. Every event with $A_{\max} \sim 50$ will enjoy these advantages and offer the prospect of detecting sub-Earths close to the *Einstein* ring if they are sufficiently abundant.

6 SIMULATION

To further quantify the detectability of low-mass planets in events of moderately high magnification, a sample of simulated events was generated and fully analysed using standard procedures. The simulation was carried out assuming follow-up telescopes with apertures larger than those presently in use become available in the future.

6.1 Simulated events

An expected distribution of events was generated by extrapolating the planetary mass function of Cassan et al. (2012) to planets with masses in the range $(1–6)\,M_\oplus$ and separations in the range 1.25–5.0 au. These ranges were subdivided into a 5×5 array as shown in Table 1.

In the table, the relationship of Cassan et al. between the microlensing parameters q and d and physical planet masses and separations was assumed, i.e. $q = 1 \times 10^{-5}$ and $d = 1$ correspond to a planet of mass $1\,M_\oplus$ at a separation 2.5 au from its host star. The numbers of planets in the paired ranges in the table are equal according to the mass function of Cassan et al. Also, the efficiencies of planet detection in these ranges are equal according to the d to $1/d$ symmetry of microlensing (Griest & Safizadeh 1998). These symmetries reduced the number of simulations that were required.

Magnification maps were constructed for the 25 mass and separation (q, d) combinations shown in Table 1. On each map 54 source star tracks were laid down with $\rho = 0.0005$, 0.001 or 0.002, $u_{\min} = \pm 0.005$, ± 0.01 or ± 0.02, and $t_E = 10$, 20 or 30 d, respectively.

Table 1. Expected number of planets per 100 stars according to the planetary mass function of Cassan et al. (2012).

	Separation (au)				
	2.25–2.5 or 2.5–2.78	2.0–2.25 or 2.78–3.13	1.75–2.0 or 3.12–3.57	1.5–1.75 or 3.57–4.17	1.25–1.5 or 4.18–5.0
	Projected separation (d)				
Mass	0.9–1.0 or 1.0–1.11	0.8–0.9 or 1.11–1.25	0.7–0.8 or 1.25–1.43	0.6–0.7 or 1.43–1.67	0.5–0.6 or 1.67–2.0
$(1-2)\,M_\oplus$	14.42	16.26	18.28	21.08	24.94
$(2-3)\,M_\oplus$	5.62	6.32	7.10	8.20	9.34
$(3-4)\,M_\oplus$	3.08	3.48	3.90	4.50	5.34
$(4-5)\,M_\oplus$	1.98	2.24	2.52	2.90	3.44
$(5-6)\,M_\oplus$	1.40	1.58	1.76	2.04	2.42

The track angle θ was held fixed at $60°$ because of the approximate independence of detection sensitivity on this parameter shown in Fig. 4 for values of $30° \leq \theta \leq 90°$. It was assumed that these source star tracks would provide a representative sample of real events observed at moderately high magnification.

Although events with *Einstein* crossing times ≥ 30 d are common (Sumi et al. 2011), we did not include them in the simulation because less than half of them would enjoy fair weather throughout their FWHM's. Also, we did not weight events with $u_{\min} = \pm 0.02$ more highly than those with $u_{\min} = \pm 0.005$. Even though the former events will occur more frequently, the requirements that the weather be clear throughout the FWHM, and that the FWHM's of consecutive events should not overlap, will favour the latter events.

The above procedure yielded 1350 light curves to which noise was added using data from the 1.8 m MOA telescope. The MOA telescope was selected for this purpose as it is best known to the authors, and because it is located in a site of less than perfect astronomical seeing. Its performance therefore provides a realistic measure of what is possible with telescopes in the 1–2 m class range.

Published analyses of several MOA events enable the data to be calibrated. The light curve of MOA-2011-BLG-293 yields delta flux values of ~ 7000 at $I = 18$ and ~ 17000 at $I = 17$ (Yee et al. 2012), MOA-2010-BLG-477 yields a delta flux value $\sim 200\,000$ at $I = 14.5$ (Bachelet et al. 2012), and MOA-2009-BLG-387 yields delta flux $\sim 12\,000$ at $I = 17.4$ and $\sim 27\,000$ at $I = 16.8$ (Batista et al. 2011). These observations that were made on different CCDs on the MOA camera yield an average scale factor of $\sim 12\,000$ delta flux units at $I = 17.5$ and $\sim 120\,000$ at $I = 15$. The latter value corresponds to a solar-like star in the Galactic bulge magnified ~ 100 times when allowance for typical extinction is included.

Examination of the above data sets also reveals that the errors at the MOA website[7] are approximately correctly normalized, and that there is a very clear demarcation between data taken in fair weather and data taken in less-than fair weather. For events with main-sequence source stars, the fair-weather data have photometry errors ~ 300 delta flux units at all but the highest magnifications. When the delta flux values reach 150 000–200 000 the errors gradually rise to 700–800.

Combining the above information, we conclude that the precision achieved by the MOA telescope in 60 s exposures taken in fair weather when solar-like stars are magnified up to ~ 200 times is $\sim 0.2 \times A^{0.2}$, where A denotes magnification. This quite accurately represents the uncertainty when $50 \leq A \leq 200$ and at lower magnifications.

Gaussian noise was added to the above sample of light curves using the above parametrization. A sampling rate of one exposure

per 0.001 d was assumed for the FWHM of each light curve, reducing to one exposure per 0.02 d out to $\pm 3t_E$, and zero thereafter. The sampling rate of one 60 s exposure per 0.001 d is regularly achieved by the MOA telescope, and it could be achieved by follow-up telescopes with smaller cameras. The sampling rate of one exposure per 0.02 d is a realistic estimate of what could occur using the combined resources of the MOA, OGLE, KMTNet and Harlingten telescopes when all are operational.

6.2 Typical light curves

The 1350 simulated light curves were analysed using a grid-minimization algorithm in which χ^2 was calculated for each combination of parameters on a grid, and the grid was moved until a minimum was found that did not use edge values of any parameter. Initial trials were randomized, and a two-step procedure of coarse steps followed by fine ones was used. The analysis procedure was verified by comparison with published analyses of several events.

Typical results for simulated events are shown in Figs 11 and 12, where low-mass planets were situated fairly close to the *Einstein* ring. Figs 13 and 14 show extreme examples with the highest mass planet studied here situated closest to the *Einstein* ring, and a
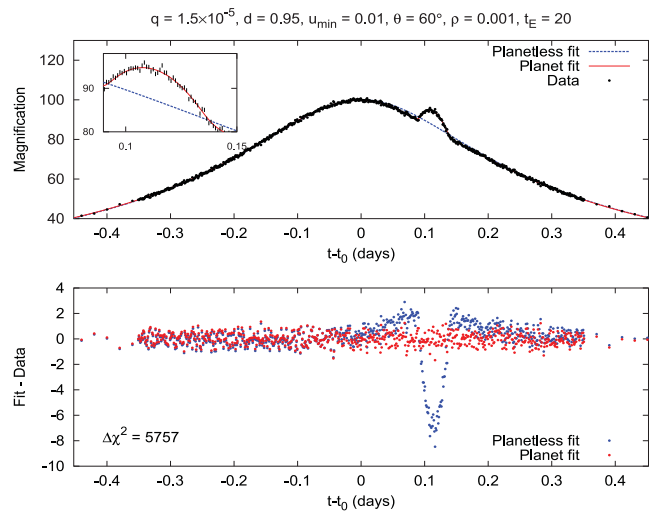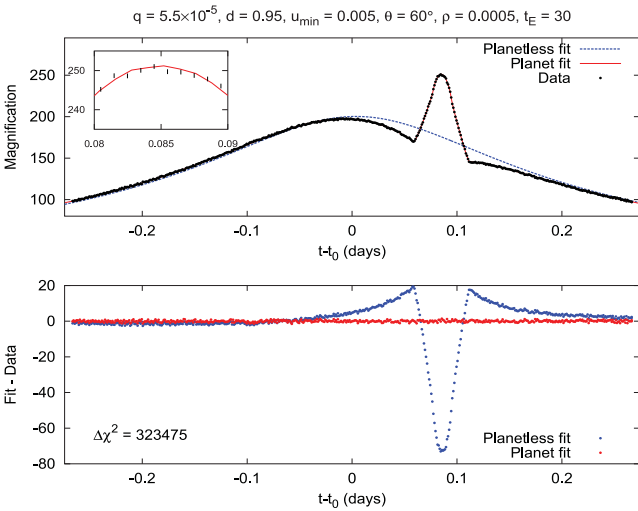

Figure 11. Best fits with and without a planet to a simulated light curve from the top left of Table 1, i.e. for the lightest planet in this study ($q = 1.5 \times 10^{-5}$) at the minimum separation from the *Einstein* ring ($d = 0.95$). The track parameters given in the header led to a clear detection with a $\Delta\chi^2 = 5757$ difference between the best fits. Most of the 54 tracks laid down on the $(q, d) = (1.5 \times 10^{-5}, 0.95)$ map yielded comparably clear detections. The average value of $\Delta\chi^2$ was 9366.

[7] https://it019909.massey.ac.nz/moa/
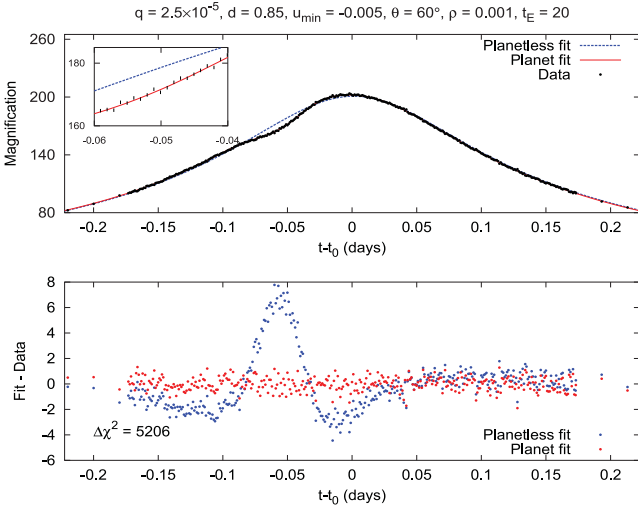
Figure 12. Best fits with and without a planet to a planet with the second lowest mass in Table 1 ($q = 2.5 \times 10^{-5}$) at the second closest position ($d = 0.85$) to the *Einstein* ring for typical track parameters. Many of the 54 tracks laid down on the $(q, d) = (2.5 \times 10^{-5}, 0.85)$ map yielded comparably clear detections.
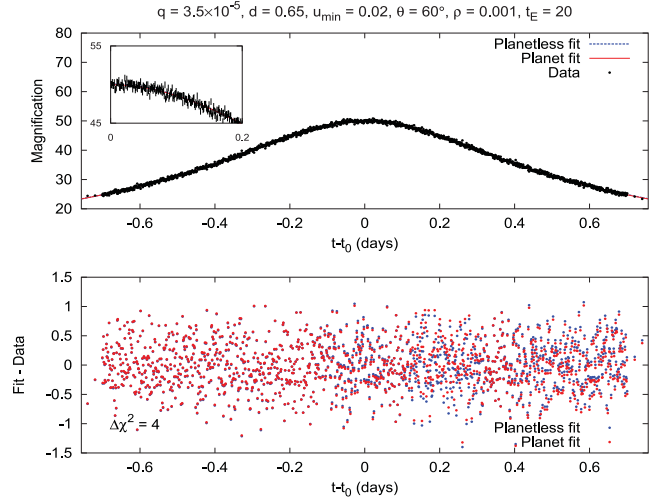

Figure 14. Undetectable signal caused by a lightish planet $q = 3.5 \times 10^{-5}$ quite far from the *Einstein* ring ($d = 0.65$).

Figure 13. Unmistakable signal caused by a 'heavy' planet with $q = 5.5 \times 10^{-5}$ close to the *Einstein* ring ($d = 0.95$).

Figure 15. Borderline signal with $\Delta\chi^2 = 304$ caused by slightly heavier planet than that shown in Fig. 13 slightly closer to the *Einstein* ring. The planetary deviation is ∼2 per cent, or only half the detection threshold assumed in Fig. 5.

low-mass planet situated far from the ring. The former case leads to a very clear detection ($\Delta\chi^2 = 323\,475$), the latter to no detection ($\Delta\chi^2 = 4$). Finally, Fig. 15 shows an example of a borderline detection with $\Delta\chi^2 \sim 300$.
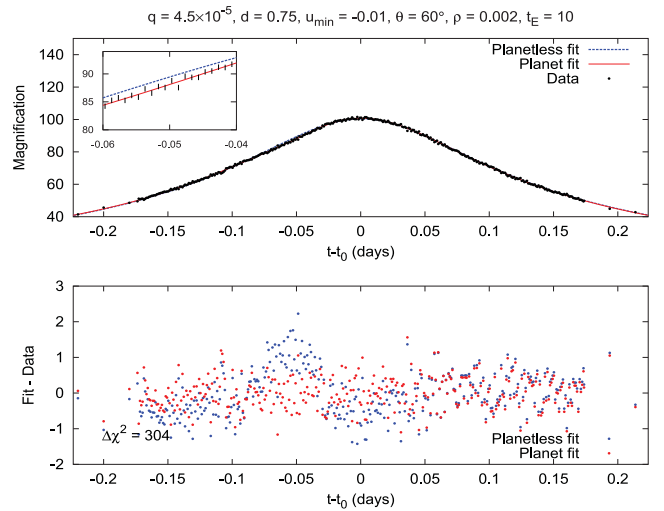
6.3 Critical $\Delta\chi^2$ for planet detection

Several light curves with $\Delta\chi^2 \sim 300$ were examined by eye to determine a reasonable minimum value of this parameter required for planet detection. Three examples are shown in Fig. 16 with $\Delta\chi^2 \leq 300$ and three with $\Delta\chi^2 \geq 300$ in Fig. 17. On the basis of these trials, we set $\Delta\chi^2 = 300$ as the minimum value required for detection in our simulation.

This value was chosen for the 'ideal' experiment mentioned above, with identical, robotically controlled 1–2 m telescopes oper-

ating in sites of excellent seeing producing an ensemble of events for joint analysis. It may not be realized in practice. Yee et al. (2013) concluded from an examination of events being monitored with current facilities that $\Delta\chi^2 = 500$ is a more plausible threshold.

We note that, if we had chosen the latter threshold in the simulation that follows, the results would not have changed much. Most detections in our simulation have $\Delta\chi^2 \geq 1000$. In Table 2 that follows, the detection efficiencies for $(1-2)\,M_\oplus$ planets at the first two separations would fall from 0.67 to 0.66 and from 0.36 to 0.26, respectively. Likewise, the efficiencies for $(2-3)M_\oplus$ planets at the first two separations would fall from 0.67 to 0.67 (no change) and from 0.53 to 0.44, respectively.
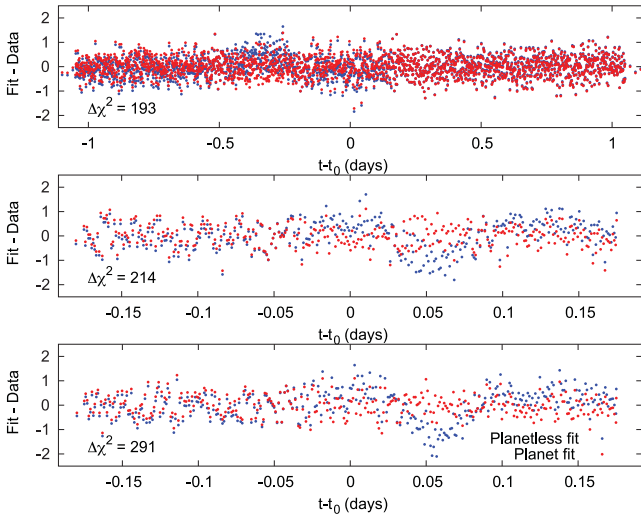
Figure 16. Typical planetary deviations with $100 \leq \Delta\chi^2 \leq 300$.
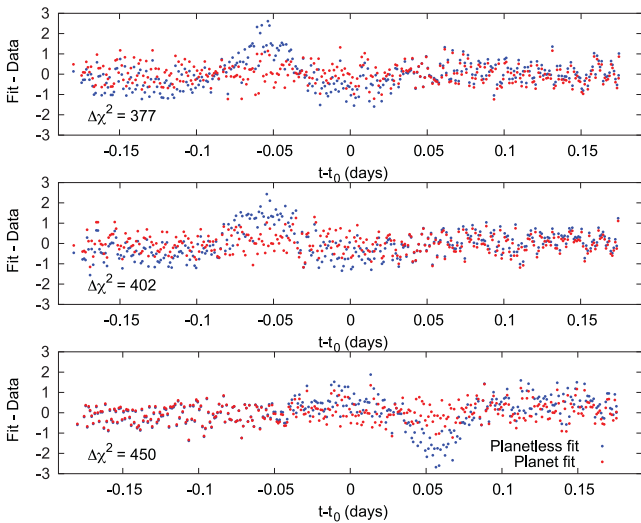
Figure 17. Typical planetary deviations with $300 \leq \Delta\chi^2 \leq 500$.

6.4 Planet-detection efficiency

For each map with (q, d) values given in Table 1, the value of $\Delta\chi^2$ for each of the 54 source star tracks was calculated. An efficiency for planet detection for a given map was determined as 0.67 times the fraction of tracks with $\Delta\chi^2 \geq 300$, where the factor 0.67 was included because only those planets at angles $\geq 30°$ are detected during the FWHM (Rattenbury et al. 2002). This yielded the results shown in Table 2. This table also includes the estimated number of detections in each (q, d) interval per 100 stars based on the planetary mass function of Cassan et al. (2012).

It is evident from Table 2, that if some tens of events with moderate magnifications were monitored, and if the planetary mass function of Cassan et al. is approximately valid, then measurements of relatively good statistical precision could be made of the abundance of planets with a few Earth masses.

7 DISCUSSION

There are a large number of variables that differentiate one gravitational microlensing event from another. It is difficult to allow for every possible contingency even when discussing just one particular characteristic such as planet-detection efficiency. In the preceding sections, we considered those variables whose values are most likely to affect the detectability of low-mass planets in microlensing events of high magnification. We focused in particular on the peak value of the magnification A_{max}, but also considered results for various values of the source-size parameter ρ and the *Einstein* radius crossing time t_E. These variables are the only ones whose magnitudes are likely to be known with any degree of confidence prior to an event reaching peak magnification. On the basis of their values, decisions may be made on whether or not to observe an event intensively.

We have found that events with $50 \leq A_{max} \leq 200$, $0.0005 \leq \rho \leq 0.002$ and $10 \leq t_E \leq 30$ d, offer a sensitive hunting ground for low-mass planets provided their FWHM's are monitored continuously with 1–2 m class telescopes. The frequency of such events should enable selections to be made to avoid troublesome events such as those with variable or potentially spotty source stars, peak data taken partly in poor weather or under moonlight, or those with nearby bright stars.

7.1 Accuracy of planetary characterization

The planetary perturbations shown in the preceding sections are relatively featureless. It might therefore appear difficult to distinguish a perturbation caused by a light planet close to the *Einstein* ring from that of a heavy planet further away. To quantify this effect, we examined the accuracy with which planets could be recovered from their simulated light curves.
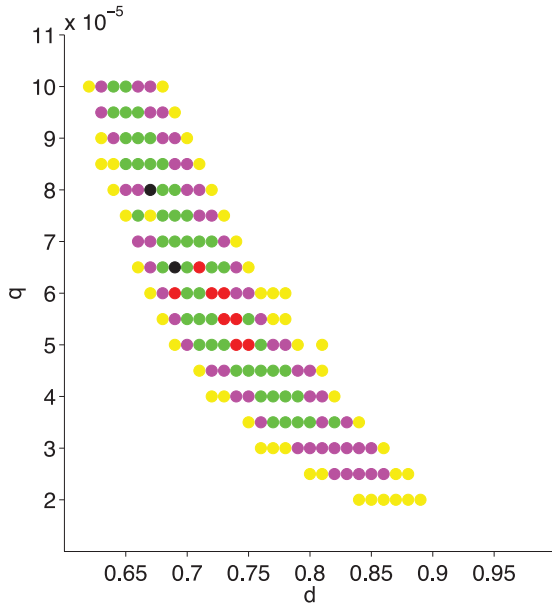
Fig. 18 shows χ^2 as a function of q and d for the light curve shown in Fig. 12 in which $\Delta\chi^2$ was 5206. In this case, the uncertainties in q and d are seen to be ± 10 per cent and ± 3 per cent at the 3σ level,

Table 2. Efficiency of planet detection in microlensing events of moderately high magnification for planets of various masses and separations. The number of detections per 100 stars according to the planetary mass function of Cassan et al (2012) is shown in parentheses.

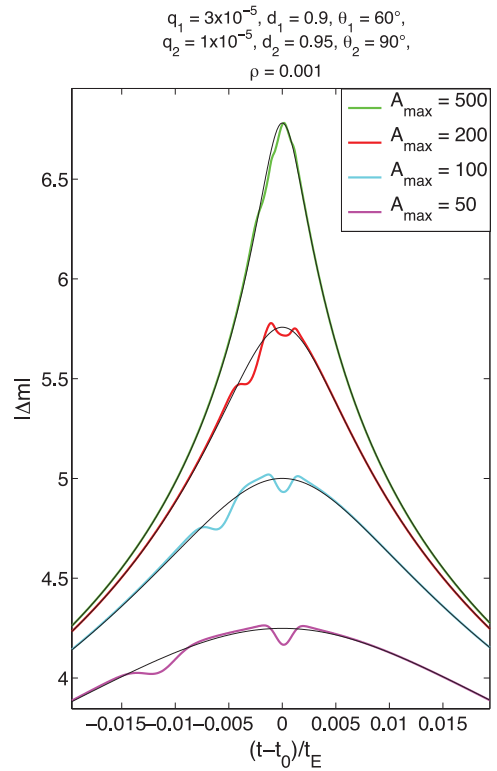|	Separation (au)				
	2.25–2.5 or 2.5–2.78	2.0–2.25 or 2.78–3.13	1.75–2.0 or 3.12–3.57	1.5–1.75 or 3.57–4.17	1.25–1.5 or 4.18–5.0
	Projected separation (d)				
Mass	0.9–1.0 or 1.0–1.11	0.8–0.9 or 1.11–1.25	0.7–0.8 or 1.25–1.43	0.6–0.7 or 1.43–1.67	0.5–0.6 or 1.67–2.0
$(1-2) M_{\oplus}$	0.67 (9.62)	0.36 (5.82)	0.11 (2.03)	0.0 (0.0)	0.0 (0.0)
$(2-3) M_{\oplus}$	0.67 (3.75)	0.53 (3.36)	0.23 (1.67)	0.04 (0.30)	0.0 (0.0)
$(3-4) M_{\oplus}$	0.67 (2.05)	0.62 (2.15)	0.36 (1.40)	0.12 (0.55)	0.0 (0.0)
$(4-5) M_{\oplus}$	0.67 (1.32)	0.65 (1.46)	0.42 (1.06)	0.20 (0.57)	0.01 (0.04)
$(5-6) M_{\oplus}$	0.67 (0.94)	0.67 (1.05)	0.44 (0.78)	0.23 (0.48)	0.06 (0.15)
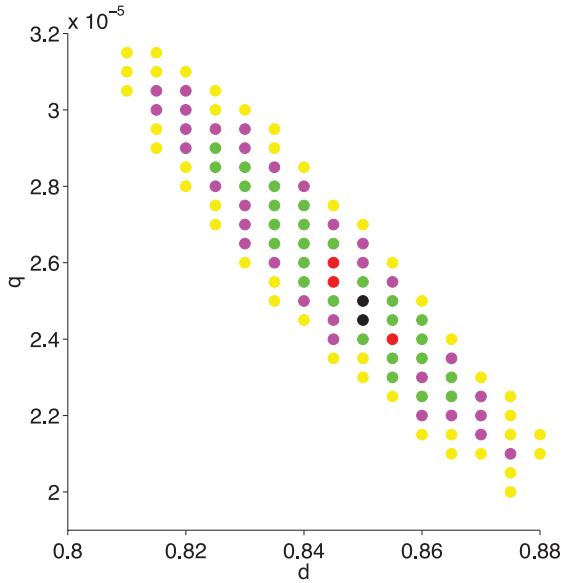
Figure 18. χ^2 as a function of q and d for the event shown in Fig. 12 with $\Delta\chi^2 = 5206$. 1σ, 2σ, 3σ, 4σ and 5σ excesses over the minimum are shown in black, red, green, purple and yellow, respectively. The known position of the planet in this event, $(q, d) = (2.5 \times 10^{-5}, 0.85)$, was well reproduced by the simulated data.

Figure 19. χ^2 as a function of q and d for the borderline detection shown in Fig. 15 with $\Delta\chi^2 = 304$. The colour code is as in Fig. 18. Some numerical noise in the simulated data is evident, and the known position of the planet, $(q, d) = (4.5 \times 10^{-5}, 0.75)$, is only approximately reproduced.

respectively. Fig. 19 shows that the uncertainties grow to ± 50 per cent and ± 10 per cent for the borderline detection in Fig. 15 with $\Delta\chi^2$ was 304. These analyses also yielded uncertainties of ± 20 per cent and ± 30 per cent for the above events at the 3σ level for the recovered value of the source-size parameter ρ.

It is apparent from the above that the richest harvest of planets will occur in events where very low-mass planets are situated close to the *Einstein* ring. This confirms the expectation given in

Figure 20. Typical planetary deviations in magnitudes for A_{max} equal to 50, 100, 200 and 500 for events with two low-mass planets. The planet-to-star mass ratios are 3×10^{-5} and 10^{-5}, respectively. Their projected separations d are 0.9 and 0.95, respectively, their position angles differ by $30°$, and the impact parameters are negative. Planetary deviations for $A_{max} = 2000$ would be imperceptible on this plot.

Section 4 that was based on the breadth of the left-hand panel of Fig. 5. It is also evident that definitive detections such as those shown in Figs 10 and 11 require the use of 1–2 m class telescopes.

7.2 Terrestrial parallax

As in other planetary detections by microlensing, measurements of orbital and/or terrestrial parallax can assist to extract absolute values of planetary masses and separations from the microlensing parameters q and d. In this regard, we note that orbital parallax is unlikely to be measurable in the events we have modelled with $t_E \leq 30$ d, but that terrestrial parallax may be measurable in some cases. The rise and fall times of the planetary perturbations shown in Fig. 3 are relatively steep, of the order of 20 min. If these perturbations were intensively monitored from different continents and/or different hemispheres it might be possible to measure terrestrial parallax in some cases. However, we note that terrestrial parallax has been measured previously in events of very high magnification only (Gould et al. 2009; Yee et al. 2009).

7.3 Multiplanet events

If two or more planetary deviations are present on a light curve, as the planetary mass function of Cassan et al. (2012) suggests could be the case when extrapolated to lower masses, it would be easier to identify the deviations if they are well separated. Two conditions must be met to achieve the above. First, the projected position

angles of the planets should differ by ∼30° or more in order for the individual deviations not be superimposed on one another, and secondly t_{FWHM} must be several times the duration of an individual planetary deviation. This translates to $A_{max} \leq 200$ approximately, as shown in Fig. 20.

We note that multiplanet events have been reported previously (Gaudi et al. 2008; Han et al. 2013) in events with magnifications 100 and 290, respectively. However, the detected planets in these cases were all giants.

8 CONCLUSION

In recent years, the microlensing community has focused attention on events with the highest observed magnifications, in particular on events with magnification ≥200 (Gould et al. 2010). As mentioned in Section 1, this resulted in the discoveries of several planets by telescopes with apertures ranging from 0.3 to 2.0 m. The detected planets have separations from their host stars of the order of a few au and correspondingly cool temperatures. Their measured masses range from a few Earth masses to a few Jupiter masses. They provide a representative sample of the distribution of planets between us and the centre of the Galaxy that orbit a relatively unbiased sample of host stars. The discoveries are important because other planetary detection techniques are insensitive to such planets. On the basis of these discoveries the first estimates of the abundances of cool planets in the Milky Way were made.

In an effort to build on these successes, we have proposed a modified procedure for extending the measurements down to Earth mass. The modified strategy makes use of the surprisingly good sensitivity of microlensing events with magnifications $50 \leq A_{max} \leq 200$ to low-mass planets situated close to the *Einstein* ring. It was found that high-quality detections of low-mass planets such as those depicted in Figs 11 and 12 could be made by densely monitoring the peaks of these events with 1–2 m class telescopes. If an extrapolation of the planetary mass function of Cassan et al. (2012) to Earth mass is approximately valid, a statistically significant sample of detections could be made by monitoring some tens of events.

In recent years ∼10 events with magnification ≥200 have been detected by the MOA and OGLE collaborations annually. The inclusion of events with A_{max} down to 50 should quadruple the event rate, and thus permit some tens of these events with moderately high magnifications to be monitored in good conditions relatively rapidly. In this way, the planetary mass function could be measured down to Earth mass. In addition, sub-Earths and planetary systems with more than one low-mass planet might be found.

Results obtained following the above procedure would provide an independent check of measurements made by monitoring events of low magnification (Kim et al. 2010) and of entirely independent results obtained from radial velocity (Howard et al. 2010; Mayor & Queloz 2012) and transit measurements (Borucki et al. 2011).

REFERENCES

Abe F. et al., 2004, Sci, 305, 1264
Bachelet E. et al., 2012, ApJ, 754, 73
Batista V. et al., 2011, A&A, 529, A102
Bennett D. P. et al., 2008, ApJ, 684, 663
Bond I. A. et al., 2002, MNRAS, 331, L19
Borucki W. et al., 2011, ApJ, 736, 19
Cassan A. et al., 2012, Nat, 481, 167
Dong S. et al., 2006, ApJ, 642, 842
Dong S. et al., 2009, ApJ, 698, 1826
Fouqué P. et al., 2010, A&A, 518, A51
Gaudi B. S., Naber M. N., Sackett P. C., 1998, ApJ, 502, L33
Gaudi B. S. et al., 2008, Sci, 319, 927
Gould A. et al., 2006, ApJ, 644, L37
Gould A. et al., 2009, ApJ, 698, L147
Gould A. et al., 2010, ApJ, 720, 1073
Griest K., Safizadeh N., 1998, ApJ, 500, 37
Han C., 2009, ApJ, 691, 452
Han C., Kim D., 2009, ApJ, 693, 1835
Han C. et al., 2013, ApJ, 762, L28
Horne K., Snodgrass C., Tsapras Y., 2009, MNRAS, 396, 2087
Howard A. et al., 2010, Sci, 330, 653
Janczek J. et al., 2010, ApJ, 711, 731
Kim S.-L. et al., 2010, in Stepp L. M., Gilmore R., Hall H. J., eds, Proc. SPIE Conf. Ser. Vol. 7733, Ground-Based and Airborne Telescopes III. SPIE, Bellingham, p. 77333
Liebes S., 1964, Phys. Rev., 133, 835
Mayor M., Queloz D., 2012, New Astron. Rev., 56, 19
Miyake N. et al., 2011, ApJ, 728, 120
Muraki Y. et al., 2011, ApJ, 741, 22
Paczynski B., 1996, ARA&A, 34, 419
Rattenbury N. J., Bond I. A., Skuljan J., Yock P. C. M., 2002, MNRAS, 335, 159
Rhie S. H. et al., 2000, ApJ, 533, 378
Sumi T. et al., 2011, Nat, 473, 349
Udalski A. et al., 2005, ApJ, 628, L109
Wambsganss J., 1997, MNRAS, 284, 172
Yee J. C. et al., 2009, ApJ, 703, 2082
Yee J. C. et al., 2012, ApJ, 755, 102
Yee J. C. et al., 2013, submitted

This paper has been typeset from a TEX/LATEX file prepared by the author.